Artificial intelligence-assisted geometry optimization of a v-shape secondary reflector for a beam-down linear Fresnel collector

Christos Sammoutos[a], Georgios Vamvouras[a], Panagiotis Lykas[a], Konstantinos Polychronakis[a], Angeliki Kitsopoulou[a], Evangelos Vidalis[a], Dimitrios N. Korres[a], Evangelos Bellos[b], Christos Tzivanidis[a]

[a] Thermal Engineering Department, School of Mechanical Engineering, National Technical University of Athens, Athens, Greece, sammoutos@mail.ntua.gr, CA, gvamvouras@mail.ntua.gr, plykas@mail.ntua.gr, polichronakis_konstantinos@mail.ntua.gr, akitsopoulou@mail.ntua.gr, evanvidalis@mail.ntua.gr, korres@central.ntua.gr, ctzivan@central.ntua.gr

[b] Department of Mechanical Engineering, School of Engineering, University of West Attica, Athens, Greece, bellose@uniwa.gr

Abstract:

Beam-down concentrating solar systems are promising technologies for exploiting solar irradiation. They consist of two consecutive reflections that redirect the solar beam to the ground where their receiver is located. Beam-down technology appears to be ideal for the utilization of solar energy for heat production, solar fuel production, and other chemical processes. One of the most crucial elements of such systems is the geometry of the secondary reflector since it significantly affects their overall efficiency. However, the optimization process for such systems is time-consuming, and it must be processed individually for every deviation of the primary mirror field. In this work, a novel v-shape secondary reflector for a beam-down linear Fresnel collector is proposed, aiming to combine the benefits of both the flat and the hyperboloid secondary reflectors. An optical investigation of the system is presented to calculate the optical efficiency. Furthermore, the optimal geometry of this reflector for various primary mirror fields' configurations is presented. To reduce the optimization process time, a heuristic optimization algorithm based on Optuna's Tree-structured Parzen Estimator (TPE) sampler is employed to determine the optimal geometry of the secondary reflector for additional primary mirror field arrangements, considering different numbers of primary mirrors and various distances between consecutive mirrors. Moreover, artificial intelligence is utilized as an online metamodel trained on completed Optuna trials to further accelerate the optimization by substituting the slower primary solver in a portion of evaluations. The maximum optical efficiency of the system is equal to 55.48%, whereas the maximum value of the intercept factor between the primary mirror field and the secondary reflector is equal to 98.9%, and the maximum value of the intercept factor between the secondary reflector and the receiver is equal to 73.3%. The optimization time using Optuna's TPE was the 10.6% of the time using the parametric analysis.

Keywords:

Artificial intelligence-assisted optimization; Beam-down linear Fresnel reflector; Optical analysis; V-shape secondary reflector.

1. Introduction

The energy issue is among the most important challenges humanity must face in the near future, including the production, storage, and security of supply [1]. This issue is becoming more intense in regions that have high dependence on fossil fuel supply by third parties, leaving them exposed to countries that control the natural reservoirs. Thus, new energy sources and technologies to exploit are mandatory for energy security. Utilizing Renewable energy sources seem to be the most promising pathway towards tackling these issues since they can provide sustainable and environmentally friendly solutions. The main RES are solar, hydro, wind, biomass, geothermal, and biomass [2]. Among them, solar energy is undoubtedly the most promising one due to its significant solar potential that can be exploited worldwide.

Solar energy can be exploited for industrial or household applications both for heat and electricity production. Industries require energy in the form of electricity and heat to operate for various processes [3], whereas buildings for daily applications such as space heating and cooling. For buildings, non-concentrating solar technologies are utilized to cover their energy demand. For household applications demanding electricity, Photovoltaics (PVs) are undoubtedly the most dominant technology, including some variations such as the building integrated PVs or the building adopted PVs. For domestic hot water and other heat needs, such as heating of spaces, Flat Plate Collectors (FPCs) or Evacuated Tube Collectors (ETCs) are exploited. However,

these technologies are limited regarding the maximum temperature levels that can be achieved, mainly in the temperature range of 30°C to 200°C, and cannot provide solutions for industrial applications demanding heat in higher temperature levels [4].
To achieve higher temperature levels, higher concentration ratios must be achieved. Thus, solar concentrating technologies are exploited using reflective surfaces as concentrators to focus the solar irradiation on a smaller surface. The most common Concentrated Solar Power (CSP) technologies are, in ascending order based on the maximum indicative temperature levels they can achieve, the Compound Parabolic Collectors (CPCs) for temperatures up to 240°C, the Linear Fresnel Reflectors (LFRs) up to 250°C, the Parabolic Trough Collectors (PTCs) up to 400°C, the Parabolic Dish Collectors (PDCs) up to 1500°C, and the Solar Towers (STs) up to 2000°C [4]. It has to be mentioned though that in existing power production facilities utilizing PDCs or STs, the operating temperature ranges are significantly lower than their maximum theoretical potential. CSP system's most significant advantage, except from utilizing solar energy, is that they can be coupled with Thermal Energy Storage (TES) systems improving the dispatchability of the produced energy. This provides a huge advantage over technologies producing electricity that are bound to storage solutions such as batteries which are not environmentally friendly and their main materials for construction can be found in specific regions [5]. Despite their significant improvement in terms of reliability, safety, and overall investment and maintenance cost, CSP still struggle to compete other technologies utilizing RES since they still have a relatively higher levelized cost of energy. Thus, improvements on the design and operation of such systems have to be investigated.
In this direction, a new CSP technology has been investigated over the last few years, known as the Beam-Down (BD) CSP technology. The main difference between BD and conventional CSP is that the BD design consists of an extra reflector, and the receiver is located on the ground [6]. This design provides some critical advantages over the conventional CSP. First of all, the receiver remains stable and does not rotate or move thus increasing its reliability. Additionally, the safety levels of these systems are enhanced due to the location of the receiver, and, as a result, the exploitation of chemical reactors or fluidized beds is more feasible. Also, pumping demand is significantly reduced, as well as the length of the piping configuration. Moreover, the total height of the system is reduced, which leads to less constructive materials and wind loads [6]. As a result, the total constructive cost of BD systems compared to conventional CSP is reduced, and at the same time, the reliability is increased. In the literature, there is some research conducted referring to the BD systems. Xu et al. [7] modeled a BD solar dish with a fixed secondary reflector, and the maximum overall efficiency was 79.0%, whereas Mokhtar et al. [8] calculated the overall efficiency of the BD solar tower at 28.0%. Taramona et al. [9] designed a flat BD Linear Fresnel Reflector (BDLFR) with a flat secondary reflector for further cost reduction, whereas Sammoutos et al. [10] investigated a parabolic secondary receiver for enhanced optical efficiency. The previous solutions for the secondary receiver emphasize on the simultaneous reduction of the construction cost and the improvement of the system's performance. Furthermore, designing and optimizing these reflectors is time consuming and requires high computational cost.
In this study, a novel v-shape secondary reflector is designed and optimized for maximum system optical performance, aiming to combine the advantages of low construction cost that the flat reflector provides with the superior optical efficiency provided by the hyperboloid one. Furthermore, to reduce the simulation time and computational cost, the Optuna's Tree-structured Parzen Estimator (TPE) sampler is utilized. A complete optical analysis for this novel BDLFR collector is conducted to calculate the efficiency curves for various configurations of the primary mirror field. Then, the simulation data are utilized for comparing the parametric analysis with the results obtained by using the TPE sampler aiming to prove significant computational cost reduction. To the best of our knowledge, there is no other similar study in the literature investigating such a design for a secondary reflector and also using artificial intelligence tools for reducing the computational time and cost.

2. Materials and Methods

2.1. Design of the beam-down collector

In this section, the design of the BDLFR collector is presented in detail where the emphasis is given on the design of the secondary reflector. The collector consists of three major sections, namely the primary mirror field, the secondary reflector, and the receiver which is an absorbent plate. The primary mirror field initially consists of twenty-eight mirrors. However, the effect of the total number of primary rows on the total absorbed heat and the overall optical performance is also examined. The secondary reflector has a v-shape geometry to combine low construction cost and high optical performance.

The primary mirror field consists of conventional flat linear Fresnel reflectors. These reflectors reflect the solar rays to reach the secondary reflector, which is not necessarily located at the focal point of the primary field. For hyperboloid geometries, meaning that their cavity faces the sky, the reflector is placed at a lower height compared to the receiver of the conventional LFR, and for ellipsoidal at a higher [6]. These mirrors are free to rotate so that they follow the sun's path. The solar rays reaching the furthest mirror rows, which are the furthest from the center point of the solar field, must reach the secondary reflector after being reflected symmetrically

[11]. The first row of mirrors should be placed as close to the center of the solar field as possible, taking into consideration the placement of the receiver and the shading effect due to the secondary reflector. The primary mirrors are placed equidistant, and the field is North-South oriented with an East-West tracking system. In the examined configuration, the flat mirrors are equidistant, and the distance between two consecutive mirrors is (D_{prim}) 300 mm. The only exception regards the mirrors which are closest to the center of the solar field. The distance between the first two primary mirror rows, the eastern and the western ones, is 1200 mm. Thus, there is enough space for the placement of the receiver, whose total width is equal to 900 mm. Each primary mirror has a width (W_{prim}) of 160 mm, and a thickness of is 20 mm to ensure structural integrity. The reflectance of each primary mirror (ρ_{prim}) is 0.94 [12]. The focal length of the primary mirror field (F) is 2000 mm. The total length of the primary mirror field (L) is 8000 mm, and its total width (W_{tot}) is 9016 mm. The slope angle of the primary reflectors is calculated as for the conventional linear Fresnel reflectors since they have exactly the same configuration.

The secondary reflector has a v-shape profile. To fully define the geometry and position of the reflector, several parameters have to be selected. The length of the secondary reflector is the same as the length of the primary mirror field, and its starting and ending points are the same as for a primary mirror row. The thickness of the mirror is 30 mm. This is an indicative value which does not directly affect the optical investigation presented on this work. The most significant design parameters are the slope angle of the triangle that is formed due to its shape (x_1), the aperture width of the cavity of the reflector (x_2), and finally the height of the reflector's lower point, which is the vertex of the triangle, from the ground (x_3). By specifying these parameters, the secondary reflector is fully defined. **Figure 1** illustrates these design parameters for the convenience of the reader. The reflectance of the secondary reflector is equal to 0.94, which is the same value as for the primary mirrors.

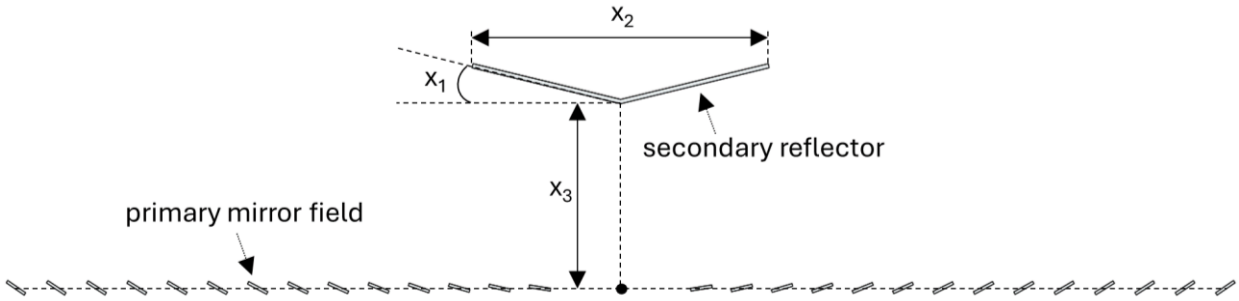

***Figure 1**. The main design parameters for the v-shape secondary reflector.*

The receiver in this study is a simple flat absorbent plate. This receiver is selected in order to minimize the simulation time by avoiding complex receiver geometries which lead to more complex computational mesh. The length of the receiver is the same as the length of the primary mirror field, and its width (W_{rec}) is equal to 900 mm, leading to an aperture area of 7.2 m^2. The absorptance and emissivity of the receiver are equal to 0.83 and 0.10 respectively, which are reasonable values based on the literature [13].

2.2. Mathematical modelling

In this section, all the necessary equations for the design and analysis of the proposed BDLFR collector are presented in detail. First of all, the geometrical analysis presents the equations needed to design the primary mirror field. The net aperture area of the primary field (A_a) is given by **Eq. (1)**, and it is the product of the length of the field (L), the width of a single primary mirror (W_{prim}), and the number of primary mirrors (N_{prim}).

$$A_a = L \cdot W_{prim} \cdot N_{prim} \quad (1)$$

The total land area (A_{tot}) required for the placement of the collector is larger than the net aperture one and it is given by **Eq. (2)**, and is calculated as the product of the length of the field, and the sum of the total field width (W) plus the width of a single primary mirror (W_{prim}) which stands for half the width of each outer mirror of the field.

$$A_{tot} = L \cdot (W + W_{prim}) \quad (2)$$

The focal distance for each primary mirror (F_j) is calculated by **Eq. (3)** right below using the focal point of the primary field (F), the distance between two consecutive mirrors (D_{prim}) and the number of each mirror (j). It has to be clarified that the secondary mirror will not be mandatorily placed on the focal point of the field as the receiver of a conventional LFR should be placed.

$$F_j = \sqrt{F^2 + (D_{prim} \cdot j)^2} \quad (3)$$

The position angle (y_j) for each primary mirror is the angle formed between the vertical axis of symmetry of the collector and the imaginary line connecting the center of a mirror and the focal point, and it is calculated using **Eq. (4)** using the number of each mirror (j), the distance between consecutive mirrors (D_{prim}) and the focal point (F).

$$y_j = \cos^{-1}\left[1 + j^2 \cdot \left(\frac{D_{prim}}{F}\right)^2\right]^{-1/2} \quad (4)$$

The slope angle (ψ_j) is the angle that is formed between the horizontal plane and each primary mirror. It is given by **Eq. (5)** right below using the position angle (y_j) and the transversal incident angle (θ_T). The "minus" sign is valid for the west oriented primary mirrors, and the "plus" sign is valid for the east oriented mirrors.

$$\psi_j = \frac{y_j \pm \theta_T}{2} \quad (5)$$

To better understand all the aforementioned geometrical parameters, **Figure 2** illustrates these variables. It has to also be mentioned that the number of each mirror is in reverse order starting from the most outer one for each side. Furthermore, the first row of mirrors should have been also placed if the primary field was used for a conventional LFR. However, in order for the receiver of the BDLFR system to be placed on the ground, the first row from each side have to be removed. Thus, the number of each primary mirror (j) takes values from two to fifteen for a total of twenty-eight primary mirrors, fourteen mirrors each side.

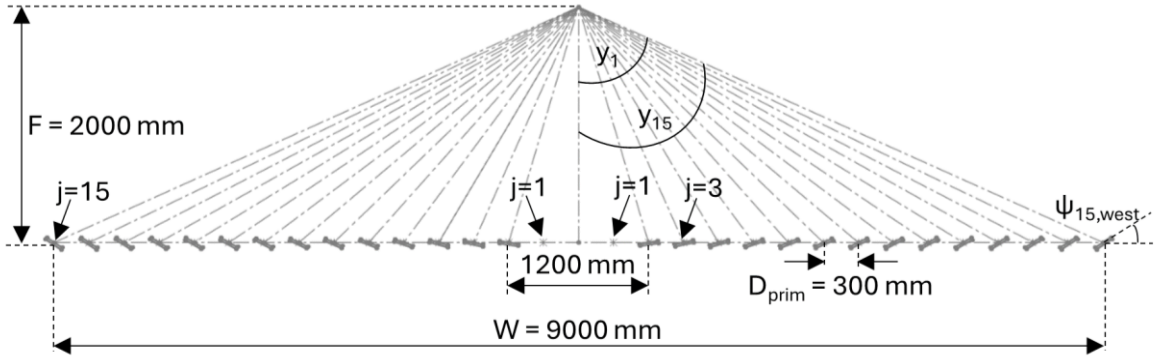

***Figure 2**. Geometrical parameters of the primary mirror field for the BDLFR collector.*

For the optical analysis, for different parameters have to be defined in order for the analysis to be completed. First of all, the optical efficiency (η_{opt}) and the Incident Angle Modifier (IAM) are fundamental parameters for solar concentrating systems. Furthermore, the intercept factor is also important. However, in BDLFR collectors, due to the extra secondary reflection, two different intercept factors have to be calculated. The first one is the intercept factor between the primary and the secondary mirrors (γ_{prim}) while the second one is the intercept factor between the secondary mirror and the receiver (γ_{sec}). The available solar energy (Q_{sol}) is calculated by **Eq. (6)** as the product of the net aperture area (A_a) and the available Direct Normal Irradiation (DNI). The optical efficiency (η_{opt}), given by **Eq. (7)**, is calculated as the quotient of the absorbed heat flux (Q_{abs}) and the available solar energy (Q_{sol}). The absorbed heat flux is the result of the simulation analysis.

$$Q_{sol} = A_a \cdot DNI \quad (6)$$

$$\eta_{opt} = \frac{Q_{abs}}{Q_{sol}} \quad (7)$$

The Incident Angle Modifier (IAM) is calculated using the **Eq. (8)** as the quotient of the optical efficiency and its maximum value. The maximum optical performance occurs when both the incident angles in the transversal (θ_T) and longitudinal (θ_L) directions are equal to zero, and the solar irradiation falls vertically on the collector.

$$IAM = \frac{\eta_{opt}(\theta_T, \theta_L)}{\eta_{opt}(\theta_T=0, \theta_L=0)} \quad (8)$$

To calculate the intercept factors, the Number of Solar Rays (NoSR) reaching its surface have to be calculated separately. Thus, different simulation scenarios where the mirror surfaces are either absorbing or reflecting the solar irradiation must ne examined. To calculate the intercept factor between the primary and secondary mirrors (γ_{prim}), the primary mirrors are set as symmetrically reflecting surfaces whereas the secondary mirror as an absorbent surface. This allows to estimate the Number of Solar Rays reaching the secondary reflector ($NoSR_{sec}$). To calculate the rays reaching the primary mirror field ($NoSR_{prim}$), the primary mirrors must be set as absorbent surfaces. Finally, to calculate the solar rays reaching the receiver ($NoSR_{rec}$), all the mirrors must reflect the solar irradiation symmetrically while the receiver should absorb them. It has to be clarified that by reflective or absorbent surfaces it is not meant that they are reflecting or absorbing the solar irradiation with factors equal to one. **Eq. (9)** calculates the intercept factor between the primary and secondary reflectors, while **Eq. (10)** between the secondary mirror and the receiver.

$$\gamma_{prim} = \frac{NoSR_{sec}}{NoSR_{prim}} \quad (9)$$

$$\gamma_{sec} = \frac{NoSR_{sec}}{NoSR_{rec}} \quad (10)$$

2.3. Artificial intelligence-assisted optimization process

In this section, the optimization process using the TPE sampler is described. The goal of this process is to identify the geometric configuration of the secondary reflector that leads to the maximum optical performance for the system, quantified through the absorbed heat flux (Q_{abs}) of the receiver. The approach combines parametric geometry generation, high-fidelity simulation, and a sequential model-based optimization algorithm. The simulation model is treated as a black-box evaluator, meaning that no analytical relationship between the design variables and the objective function is assumed. Instead, candidate designs are iteratively proposed, evaluated through simulation, and used to guide subsequent search decisions.

The design variables selected for this process are the parameters that fully define the geometry and position of the secondary reflector as presented in **Section 2.1**. Each design variable is constrained within physically meaningful bounds derived from engineering considerations. Specifically for this study, the boundaries were narrowed down to investigate the optimization potential of this strategy, while the previously conducted parametric study to determine the actual optimum geometry was more thorough. These parameters define a three-dimensional design space within which the optimization is performed. For each candidate design, the selected parameter values are written to a configuration file that is subsequently used by the simulation workflow. The simulation evaluates the system response and returns the resulting value of the absorbed heat flux (Q_{abs}), which serves as the scalar objective function value associated with that design.

The optimization process is implemented using the Optuna framework, which provides efficient algorithms for sequential optimization of expensive black-box functions. The TPE sampler is employed to generate candidate solutions. TPE belongs to the class of Bayesian-inspired optimization methods and is particularly well suited for problems where objective function evaluations are computationally expensive and gradient information is unavailable. Rather than constructing a global surrogate model of the objective function, the TPE method models the probability distributions of parameter values associated with good and poor objective outcomes. After a number of completed trials, the algorithm partitions the evaluated samples into two groups based on their objective values. A probabilistic density model is then fitted for each group. New candidate parameter sets are generated by sampling from regions of the parameter space that maximize the ratio between the density of good samples and the density of poorer samples. In practice, this strategy directs the search toward parameter regions that are statistically associated with improved performance while still maintaining a degree of exploration of unexplored areas of the design space.

The optimization begins with a number of exploratory trials that allow the algorithm to gather initial information about the response surface. In addition, several warm-start configurations are introduced near a baseline design to guide the early search toward physically realistic regions of the parameter space. These initial samples consist of small perturbations around nominal parameter values and provide the optimizer with early performance information in the neighbourhood of an existing engineering design. Each optimization trial proceeds by generating a candidate set of geometric parameters, executing the simulation workflow for that configuration, and extracting the resulting absorbed heat flux (Q_{abs}) value from the simulation output. The parameter set and the corresponding objective value are recorded in a persistent database, allowing the full history of the optimization process to be stored and enabling the study to be resumed in case of interruption. To ensure the robustness of the optimization procedure, trials that fail due to simulation errors or exceed predefined runtime limits are automatically discarded. This prevents unstable or infeasible configurations from influencing the optimization process and allows the search to proceed without manual intervention. After completion of the predefined number of trials, the parameter combination corresponding to the best observed objective value is identified as the optimal configuration. **Figure 3** depicts the optimization process utilized in this work based on the Optuna TPE. Then, the associated design parameters are exported for subsequent verification and further analysis. Through the combination of simulation-based evaluation and adaptive probabilistic sampling, the proposed workflow enables efficient exploration of the design space while minimizing the number of expensive simulation runs required.

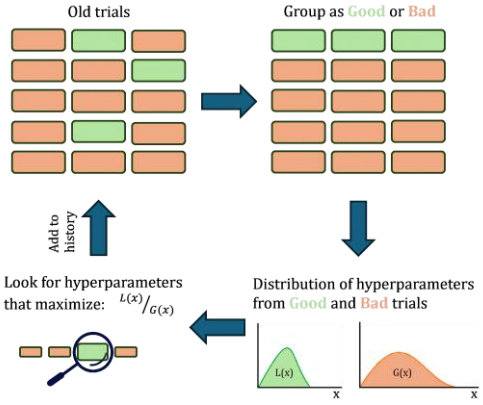

***Figure 3**. An illustration of the optimization process based on the Optuna TPE utilized in this study.*

2.4. Simulation strategy

In this section, the complete simulation methodology is presented in detail. The proposed BDLFR system has been designed using the SolidWorks 2024 software, and the optical analysis was conducted using the SolidWorks Flow Simulation toolbox [14]. This software was previously used for similar studies for conventional CSP systems such as LFR [15], PTC [16], and PDC [17]. Furthermore, this toolbox was also used for the optical and thermal analysis of a BDLFR system with a parabolic secondary reflector in our previous study [10]. Additionally, the SolidWorks software was also validated with experimental results for a conventional LFR system [18]. These studies reveal the software as a credible and reliable tool for simulating CSP systems. In this work, a BDLFR collector with a v-shape secondary reflector is investigated in optical terms. **Figure 4** presents the BDLFR collector in the software environment.

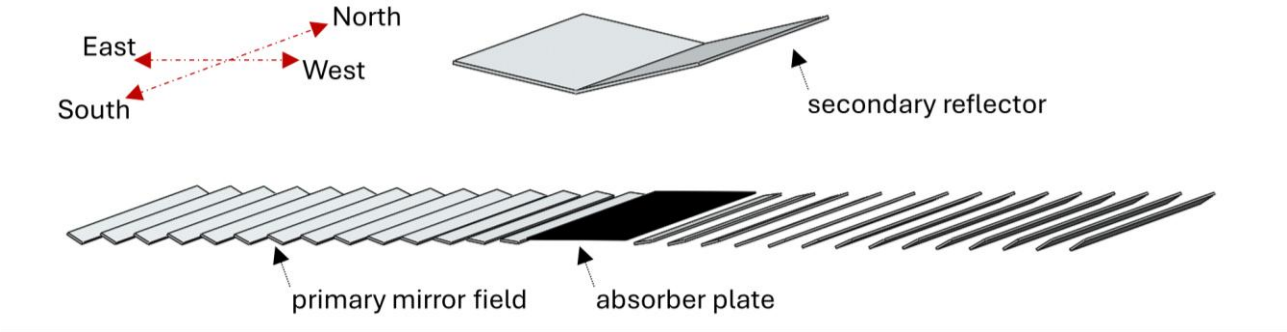

***Figure 4**. The examined BDLFR collector.*

For the optical investigation, the required simulation parameters are classified into two categories. The first category refers to the parameters that are set prior the optimization process and remain constant during this procedure. These parameters are the optical properties of the system components, the number of primary mirrors, the absorptance, and the emissivity of the receiver. On the other hand, the second category of parameters refers to the ones that vary during the optimization process. These parameters are the three design variables of the secondary reflector defined in **Section 2.1**. The simulation parameters and their simulation steps are presented in **Table 1**.

***Table 1**. Simulation parameters for the parametric analysis for the optimization process.*

Constant simulation parameters		**Variable simulation parameters**	
Incident angle (θ_T) [deg]	0.0	**Slope angle (x_1)**	10.0° to 20.0° (step 1.0°)
Direct normal irradiation [W/m^2]	1000.0	**Aperture width (x_2)**	2200 mm to 2400 mm (step 20 mm)
Absorptance (α) [-]	0.83	**Height (x_3)**	1240 mm to 1350 mm (step 10 mm)

Before conducting the simulations, an independent analysis in two levels is conducted. The first level regards the grid, meaning the number of total cells selected. The second level regards the number of solar rays falling into the aperture of the computational domain. **Table 2** presents the mesh independency analysis, and **Table 3** the sensitivity analysis for the number of solar rays. The selected number of cells is equal to 4.64 million cells, and the selected number of solar rays is 2.00 million rays. It is important to clarify that, for the number of cells, the most critical factor is the refinement level on the surfaces of the mirrors and the absorber and not just the total number. This analysis was conducted for a DNI value of 1000 W/m^2 and zero-incident angles.

***Table 2**. Mesh independency analysis.*

Parameter	**Trial 1**	**Trial 2**	**Trial 3**	**Trial 4**	**Trial 5**
Cells [x10^6]	0.24	1.39	2.51	4.59	6.56
η_{opt} [%]	49.4	56.2	55.1	55.2	55.2

***Table 3**. Sensitivity analysis for the number of solar rays.*

Parameter	**Trial 1**	**Trial 2**	**Trail 3**	**Trial 4**	**Trial 5**
Rays [x10^6]	0.10	1.00	1.50	2.00	3.00
η_{opt} [%]	54.6	55.0	55.1	55.2	55.2

The goal of the optimization process is to conclude to the optimum combination of the three design variables that result in the maximum optical efficiency for every configuration of the primary mirror field. The optimization

process is divided into two different processes. Initially, the software is used to examine all the possible combinations of the design variables. This parametric analysis allows the identification of the optimum combination. Then, the same procedure is repeated but, in this case, the TPE sampler is utilized. The sampler initially begins the parametric analysis as in the previous process. After a specific number of simulations, the sampler collects data to train its neural network aiming to bypass some of the parameter combinations that will be foreseen as unnecessary since they are unlikely to lead to the optimum optical performance. Then, these two procedures will be compared to calculate the profit in terms of computational time. The most important parameter regarding the sampler is the number of mandatory simulations that have to be conducted before starting to predict if the following design variable combinations are not potentially leading to the optimum result.

3. Results and Discussion

3.1 Optical analysis of the beam-down collector

In this section, the results regarding the optical analysis of the BDLFR collector are presented. The maximum design point was 13° for the slope angle (x_1), 2220 mm for the aperture width (x_2), and 1350 mm for the height of the reflector from the ground (x_3). The behavior of the optical efficiency against the incident angles remains the same for all the designs with minor changes mainly on the final values and not the profile. Thus, **Figure 5** presents the optical efficiency (η_{opt}), the incident angle modifier (IAM), and the intercept factors (γ_{prim}, γ_{sec}) for the case study with twenty-eight primary mirrors. It is evident that the optical performance of the system decreases as the incident angle in the longitudinal direction increases. This is reasonable considering the end losses occurring due to the size of the reflectors. The same observation is valid for the intercept factors. The maximum optical efficiency is equal to 55.48%, while the maximum primary and secondary intercept factors are equal to 98.9% and 73.3% respectively. As was expected, the maximum values are observed for zero-incident angles.

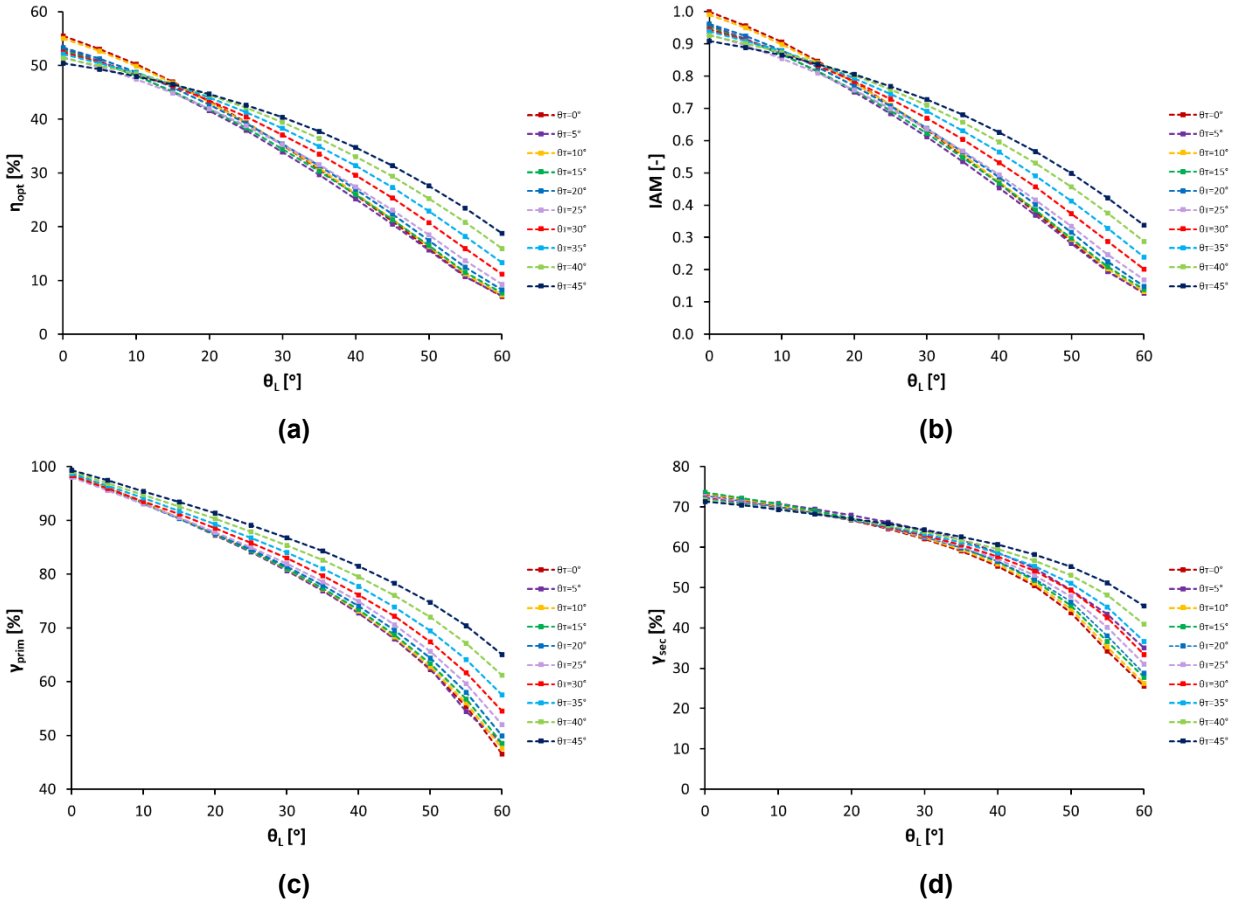

***Figure 5**. The (a) optical efficiency, (b) incident angle modifier, (c) intercept factor between the primary and secondary reflectors, and (d) intercept factor between the secondary reflector and the absorber for various incident angles in the transversal and longitudinal directions, for the primary field comprised of twenty-eight mirrors.*

On of the main scopes of this work is to reduce the computational time required for simulations regarding the design analysis of BDLFR configurations. In this direction, analytical expressions are presented right below for calculating the optical efficiency of such systems. These equations were extracted fort the constant simulation

parameters presented in **Table 2**. These equations have several terms that are combinations of multiplying coefficients (ζ_i) and the incident angles in both directions, and **Eq. (11)** is their general formulation. **Table 4** presents the values for the coefficients (ζ_i) of this equation depending on the value of the incident angle in the transversal direction, including the coefficient of determination (R^2). The values of R^2 prove that the proposed equations are estimating the optical performance of the system with quite a high accuracy.

$$\eta_{opt} = \zeta_0 + \zeta_1 \cdot \theta_T + \zeta_2 \cdot \theta_L + \zeta_3 \cdot {\theta_T}^2 + \zeta_4 \cdot {\theta_L}^2 + \zeta_5 \cdot {\theta_T}^3 + \zeta_6 \cdot {\theta_L}^3 \quad (11)$$

***Table 4**. Multiplying coefficients (ζ_i) and coefficient of determination (R^2) for various incident angles in the transversal direction (θ_T) for calculating the optical efficiency using analytical expressions.*

θ_T [deg]	Multiplying Coefficients [-]							R^2 [%]
	ζ_0	ζ_1	ζ_2	ζ_3	ζ_4	ζ_5	ζ_6	
0 to 45	51.52367	-0.13950	-0.32039	0.00795	-0.00839	$-5.42 \cdot 10^{-5}$	$3.30 \cdot 10^{-5}$	97.99
0	55.33252	0	-0.38225	0	-0.01244	0	$8.80 \cdot 10^{-5}$	99.98
15	52.70143	0	-0.34967	0	-0.01060	0	$6.39 \cdot 10^{-5}$	99.99
30	52.38440	0	-0.30985	0	-0.00702	0	$1.18 \cdot 10^{-5}$	100.0
45	50.43160	0	-0.21500	0	-0.00290	0	$-3.85 \cdot 10^{-5}$	100.0

Table 5 presents the maximum values for all the examined configurations based on the number of primary mirrors. It can be observed that the maximum optical efficiency occurs for twenty-eight primary mirrors. As the number of primary mirrors reduces, the maximum optical efficiency decreases. However, the difference is not so noticeable. **Table 6** presents the optimum values of the design variables based on the selected number of primary mirrors. The optimum aperture width (x_2) remains exactly the same for all the configurations. As the number of primary mirrors increases, the optimum slope angle (x_1) and the optimum height (x_3) increase as well. This is a reasonable result considering that the aperture width (x_2) remains the same.

***Table 5**. Maximum optical performance for each examined configuration of primary mirrors.*

Number of primary mirrors	$\eta_{opt,max}$ [%]	$\gamma_{prim,max}$ [%]	$\gamma_{sec,max}$ [%]
22	54.7	99.95	73.64
24	55.3	99.94	73.48
26	55.5	99.58	73.39
28	55.5	98.91	73.26

***Table 6.** Optimum values of the design variables resulted from the parametric analysis.*

Number of primary mirrors	Optimum slope angle (x_1) [°]	Optimum aperture width (x_2) [mm]	Optimum height (x_3) [mm]
22	10.0	2220	1310
24	11.0	2220	1320
26	12.0	2220	1340
28	13.0	2200	1350

3.2 Optimization process results

The optimization process was conducted using a Bayesian optimization framework based on the Tree-structured Parzen Estimator (TPE) algorithm, implemented through Optuna. The objective of the optimization was the maximization of the absorbed heat flux (Q_{abs}), evaluated via repeated SolidWorks flow simulations. More specifically, the objective was to minimize the negative value of the absorbed heat since SolidWorks signs as negative values the fluxes that are absorbed. The algorithm was initialized with a set of startup trials and additional warm-start samples centred around a randomly chosen nominal design, by selecting one random value for each one of the three design variables, which respected parameter boundaries, enabling both global exploration and local refinement from the early stages.

During the initial phase of the optimization, the algorithm exhibited strong exploratory behaviour. This is clearly reflected in the distribution of the sampled design points in the three-dimensional parameter space, where the values of the slope angle (x_1), the aperture width (x_2), and the height from the ground (x_3) are widely dispersed across their respective boundaries. **Figure 6** presents the distribution of the sample points for the design variables. A three-dimensional conceptual space is created by the boundary conditions set for each of the

design variable It can be observed that, initially, the sampled design points are randomly scattered across this space. Theses initial values are characterized as “older values”. Then, as the optimization process advances, the new samples are gathered in a smaller conceptual space close to the optimum solution. These samples are characterized as “newer values”.

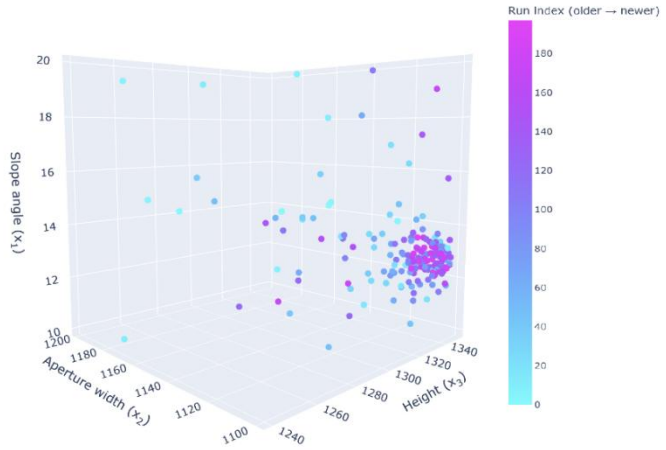

Figure 6. *The distribution of the sample points in the conceptual space of the design variables with a colour scale representing the trial number (sorted from older to newer sample points).*

The absence of clustering indicates that the surrogate model had not yet captured the structure of the objective function. This behaviour is further corroborated by the convergence plot of the absorbed heat flux (Q_{abs}), which shows significant variability in objective values, with large fluctuations and no consistent improvement trend. **Figure 7** presents the variation of the absorbed heat flux against the sampled points. Such high variance is characteristic of an exploration-dominated regime, where the algorithm prioritizes gathering information about the search space over exploiting known good regions.

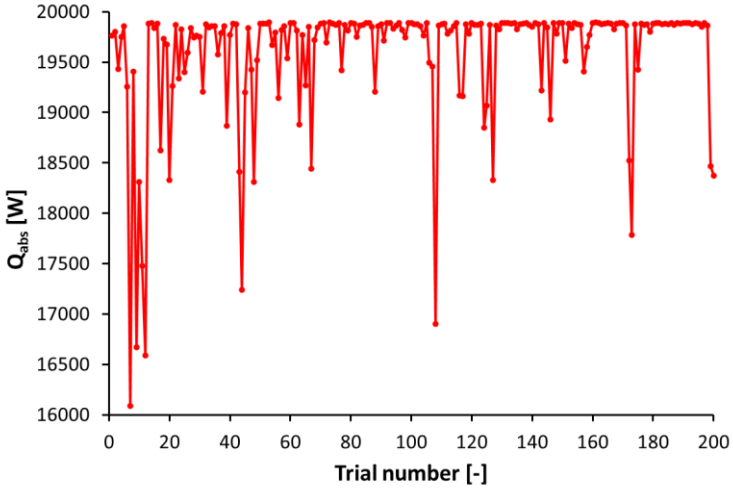

Figure 7. *The variation of the absorbed heat flux (Q_{abs}) against the trial number.*

As the number of trials increases, a clearer transition phase is observed. The Optuna’s TPE algorithm begins to construct probabilistic models distinguishing promising and non-promising regions of the parameter space. Consequently, the sampling density gradually shifted towards a narrower region. In particular, this region is around intermediate values of height from the ground (x_3) values (1320 to 1340 mm), lower aperture width (x_2) values (1110 to 1150 mm), and moderate slope angle (x_1) values (11 to 14°). This transition indicates that the algorithm is “learning” the underlying structure of the objective landscape and begins to favour regions associated with improved performance. In the later stages of the optimization process, the algorithm entered a predominantly exploitative regime. The sampled points form a dense cluster in a confined region of the parameter space, demonstrating strong convergence towards an optimal design. **Figure 7** reveals a stabilization of the objective value, with most evaluations yielding values close to the optimum absorbed heat flux (Q_{abs}). The reduction in variance and the absence of significant improvements indicate that the algorithm is refining solutions within a well-defined basin of attraction. Despite this convergence, occasional deviations from the optimal region are observed. These outliers, present in both **Figure 6** and **Figure 7**, are a result of the inherent exploration mechanism maintained by the Optuna’s TPE algorithm. This controlled exploration prevents premature convergence to suboptimal solutions and ensures robustness against local minimal.

Importantly, these exploratory steps do not significantly disrupt convergence, as the algorithm consistently returns to the optimal region. The convergence behaviour of the process suggests that the objective function exhibits a relatively smooth landscape with a clearly defined optimum, allowing the algorithm to efficiently identify and exploit the best-performing region. Overall, the optimization demonstrates a well-balanced interplay between exploration and exploitation. The algorithm initially performs extensive exploration to characterize the search space, followed by a gradual and stable transition to exploitation, where it refines the optimal solution. The absence of erratic behaviour or premature convergence indicates that the chosen optimization strategy is effective and well-suited for the problem at hand.

The results of this analysis are for the case study of twenty-eight primary mirrors. The final optimized design corresponds to a configuration with a height (x_3) equal to 1342 mm, aperture width equal to 2220 mm, and a slope angle (x_1) equal to 12.7°. This sample point leads to an absorbed heat flux (Q_{abs}) equal to 19890.9 W, and a maximum value for the optical efficiency equal to 55.48%. These results are for the case study of twenty-eight primary mirrors. It is evident that the optimum design point revealed using the Optuna's TPE algorithm is very close to the optimum point resulted from the parametric analysis presented in **Table 6**. In particular, the maximum optical efficiency is found to be slightly higher, with an increment of 0.02%. The aperture width (x_2) is exactly the same, and the slope angle (x_1) is slightly less by 0.3°. The most significant difference regards the height of the secondary reflector from the ground (x_3) which is increased by 8 mm. These small differences are acceptable considering the simulation steps of the parametric analysis while the Optuna's TPE strategy did not have this constraint, and all the values for the design variables were possible candidates.

3.3 Discussion

In this study, a beam-down linear Fresnel reflector is presented, and a novel v-shape secondary reflector is designed and optimized for the optimum optical performance. The optimum geometry of the reflector depends on the number of primary mirrors. Two optimization procedures are conducted, one based on the parametric analysis strategy, and one based on the Optuna's TPE sampler algorithm. It is evident that the proposed reflector presents adequate optical efficiency while at the same time the construction cost is reduced since there are no curves on the reflector's geometry. Using the optimization algorithm of TPE, the simulation time is significantly reduced. This results encourages the use of such methods when designing reflectors for beam down configurations. An important point of discussion regards the future research. For the TPE approach, more constraints during the optimization process could be introduced, such as considering the optimization of other variables, or considering some variables as of higher significance. Such a parameter could be the height of the reflector since it was evident that there were also other design points that, despite resulting at a lower optical performance for the system, this difference was not of great significance. Sacrificing a very small percentage of the optical efficiency, the total height of the reflector could be significantly reduced thus resulting in reduced height of the supportive construction for the reflector, and subsequently less use of supportive material and lower wind loads.

4. Conclusions

In this study, a v-shape secondary reflector for BDLFR systems is designed and optimized based on three design variables that fully define its geometry and placement. Furthermore, the Optuna's TPE sampler is used to reduce the simulation time required for the optimization process. The most important concluding points are listed below:

- The optimum geometry of the beam-down secondary reflector differs depending on the size of the primary mirror field. As the number of primary mirrors increases, the optimum value of the height of the secondary reflector increases for the same optimum aperture width, and the optimum slope angle increases as well.
- The maximum optical performance is observed when the primary mirror field consists of twenty-eight primary mirrors. The maximum optical efficiency is equal to 55.48%, whereas the maximum incident angle modifier is equal to one. The maximum value for the intercept factors between the primary and secondary reflectors, and the secondary reflector and the absorber are equal to 98.9% and 73.3% respectively.
- An analytical expression for calculating the optical efficiency of the system which consists of twenty-eight primary mirrors has been extracted from the simulation results of the parametric study. The multiplying coefficients for various functions of the optical efficiency with the incident angles in the transversal and longitudinal directions as variables have been calculated, and the minimum coefficient of determination was found to be equal to 97.99%.
- The optimum combination of the design variables resulted from the parametric analysis and from the Optuna's TPE sampler are approximately the same. The observed deviations are acceptable since they are less than the simulation step which was an input parameter for the parametric analysis. The Optuna's TPE algorithm only has the constraint of the boundary conditions, whereas for the parametric analysis there is the constraint of the simulation step.

- Using the Optuna's TPE algorithm strategy, the total simulation time is thoroughly reduced to the one tenth compared to the total simulation time for the analytical parametric study. This indicates the significance of utilizing such algorithms for the geometry optimization of the secondary reflector in beam-down systems.

Acknowledgments

The research project is implemented in the framework of H.F.R.I call "3rd Call for H.F.R.I.'s Research Projects to Support Faculty Members & Researchers" (H.F.R.I. Project Number: 23538).

Nomenclature

A	Area, m^2
D	Diameter, mm
F	Focal length, mm
L	Length, mm
N	Number
Q	Heat flux, W/m^2
R^2	Coefficient of determination
W	Width, mm
x_1	Slope angle of the secondary reflector, °
x_2	Aperture width of the secondary reflector, mm
x_3	Height of the secondary reflector from the ground, mm
y	Position angle, °

Greek symbols

α	Absorptance
γ	Intercept factor
ζ_i	Multiplying coefficient
η	Efficiency
θ_L	Longitudinal incident angle, °
θ_T	Transversal incident angle, °
ρ	Reflectance
ψ	Slope angle, °

Subscripts and superscripts

a	Aperture
abs	Absorbed
j	Number of mirror, j=[1,2,3,…,15]
opt	Optical
prim	Primary
rec	Receiver
sec	Secondary
sol	Solar
tot	Total

Abbreviations

BD	Beam-Down
BDLFR	Beam-Down Linear Fresnel Reflector
CPC	Compound Parabolic Collector
CSP	Concentrated Solar Power
ETC	Evacuated Tube Collector
FPC	Flat Plate Collector
IAM	Incident Angle Modifier
LFR	Linear Fresnel Reflector
NoSR	Number of Solar Rays

PDC Parabolic Dish Collector
PTC Parabolic Trough Collector
PV Photovoltaic
ST Solar Tower
TPE Tree-structured Parzen Estimator

References

1. Behzadi, A.; Arabkoohsar, A. Feasibility Study of a Smart Building Energy System Comprising Solar PV/T Panels and a Heat Storage Unit. *Energy* **2020**, *210*, 118528, doi:10.1016/j.energy.2020.118528.
2. Obaideen, K.; Nooman AlMallahi, M.; Alami, A.H.; Ramadan, M.; Abdelkareem, M.A.; Shehata, N.; Olabi, A.G. On the Contribution of Solar Energy to Sustainable Developments Goals: Case Study on Mohammed Bin Rashid Al Maktoum Solar Park. *International Journal of Thermofluids* **2021**, *12*, 100123, doi:10.1016/j.ijft.2021.100123.
3. Sammoutos, C.; Kitsopoulou, A.; Lykas, P.; Gonidaki, D.; Vidalis, E.; Korres, D.; Rahbari, H.R.; Tzivanidis, C.; Bellos, E. Dynamic Investigation of Thermochemical Heat Upgrade and Alternative Industrial Heating Technologies. *Energies* **2025**, *18*, 1990, doi:10.3390/en18081990.
4. Kalogirou, S. *Solar Energy Engineering: Processes and Systems*; Third edition.; Academic Press, an imprint of Elsevier: London, 2024; ISBN 978-0-323-99351-7.
5. Abdelkareem, M.A.; Ayoub, M.; Khuri, S.; Alami, A.H.; Sayed, E.T.; Deepa, T.D.; Olabi, A.G. Environmental Aspects of Batteries. *Sustainable Horizons* **2023**, *8*, 100074, doi:10.1016/j.horiz.2023.100074.
6. Bellos, E. Progress in Beam-down Solar Concentrating Systems. *Progress in Energy and Combustion Science* **2023**, *97*, 101085, doi:10.1016/j.pecs.2023.101085.
7. Xu, H.; Xu, C.; Li, S.; Zhang, Z.; Liu, Y.; Xin, T.; Yang, Y. A Beam-down Solar Concentrator with a Fixed Focus — Design and Performance Analysis. *Solar Energy* **2022**, *241*, 428–436, doi:10.1016/j.solener.2022.06.017.
8. Mokhtar, M.; Meyers, S.A.; Armstrong, P.R.; Chiesa, M. Performance of a 100 kWth Concentrated Solar Beam-Down Optical Experiment. *Journal of Solar Energy Engineering* **2014**, *136*, 041007, doi:10.1115/1.4027576.
9. Taramona, S.; González-Gómez, P.Á.; Briongos, J.V.; Gómez-Hernández, J. Designing a Flat Beam-down Linear Fresnel Reflector. *Renewable Energy* **2022**, *187*, 484–499, doi:10.1016/j.renene.2022.01.104.
10. Sammoutos, C.; Bellos, E.; Kitsopoulou, A.; Lykas, P.; Vidalis, E.; Tzivanidis, C. Optical, Thermal and Exergy Analysis of a Beam-down Linear Fresnel Reflector Coupled with a Flat Plate Receiver. *Solar Energy* **2024**, *282*, 112949, doi:10.1016/j.solener.2024.112949.
11. Taramona, S.; Gallo, A.; González-Camarillo, H.; Minio Paluello, G.; Briongos, J.V.; Gómez-Hernández, J. Beam-down Linear Fresnel Reflector Prototype: Construction and First Tests. *Renewable Energy* **2024**, *220*, 119697, doi:10.1016/j.renene.2023.119697.
12. Khandelwal, N.; Sharma, M.; Singh, O.; Shukla, A.K. Comparative Evaluation of Integrated Solar Combined Cycle Plant with Cascade Thermal Storage System for Different Heat Transfer Fluids. *Journal of Cleaner Production* **2022**, *353*, 131519, doi:10.1016/j.jclepro.2022.131519.
13. Fan, M.; You, S.; Gao, X.; Zhang, H.; Li, B.; Zheng, W.; Sun, L.; Zhou, T. A Comparative Study on the Performance of Liquid Flat-Plate Solar Collector with a New V-Corrugated Absorber. *Energy Conversion and Management* **2019**, *184*, 235–248, doi:10.1016/j.enconman.2019.01.044.
14. Mattson, J.E. *An Introduction to SOLIDWORKS Flow Simulation 2024*; SDC Publications, 2024; ISBN 978-1-63057-647-9.
15. Bellos, E.; Tzivanidis, C.; Papadopoulos, A. Daily, Monthly and Yearly Performance of a Linear Fresnel Reflector. *Solar Energy* **2018**, *173*, 517–529, doi:10.1016/j.solener.2018.08.008.
16. Korres, D.N.; Tzivanidis, C. Investigation of a Novel Small-Sized Bifacial Cavity PTC and Comparison with Conventional Configurations. *Thermal Science and Engineering Progress* **2020**, *17*, 100355, doi:10.1016/j.tsep.2019.100355.
17. Majel, B.M.; Obaid, Z.A.H.; Zidane, K. Numerical Study of the Parabolic Dish Solar Collector Performance Evaluation Using Heat Exchanger Receiver. *IJHT* **2023**, *41*, 376–384, doi:10.18280/ijht.410211.
18. Bellos, E.; Mathioulakis, E.; Tzivanidis, C.; Belessiotis, V.; Antonopoulos, K.A. Experimental and Numerical Investigation of a Linear Fresnel Solar Collector with Flat Plate Receiver. *Energy Conversion and Management* **2016**, *130*, 44–59, doi:10.1016/j.enconman.2016.10.041.